LETTER

Exponential protection of zero modes in Majorana islands

S. M. Albrecht[1]*, A. P. Higginbotham[1,2]*, M. Madsen[1], F. Kuemmeth[1], T. S. Jespersen[1], J. Nygård[1], P. Krogstrup[1] & C. M. Marcus[1]

Majorana zero modes are quasiparticle excitations in condensed matter systems that have been proposed as building blocks of fault-tolerant quantum computers[1]. They are expected to exhibit non-Abelian particle statistics, in contrast to the usual statistics of fermions and bosons, enabling quantum operations to be performed by braiding isolated modes around one another[1,2]. Quantum braiding operations are topologically protected insofar as these modes are pinned near zero energy, with the departure from zero expected to be exponentially small as the modes become spatially separated[3,4]. Following theoretical proposals[5,6], several experiments have identified signatures of Majorana modes in nanowires with proximity-induced superconductivity[7–11] and atomic chains[12], with small amounts of mode splitting potentially explained by hybridization of Majorana modes[13–15]. Here, we use Coulomb-blockade spectroscopy in an InAs nanowire segment with epitaxial aluminium, which forms a proximity-induced superconducting Coulomb island (a 'Majorana island') that is isolated from normal-metal leads by tunnel barriers, to measure the splitting of near-zero-energy Majorana modes. We observe exponential suppression of energy splitting with increasing wire length. For short devices of a few hundred nanometres, sub-gap state energies oscillate as the magnetic field is varied, as is expected for hybridized Majorana modes. Splitting decreases by a factor of about ten for each half a micrometre of increased wire length. For devices longer than about one micrometre, transport in strong magnetic fields occurs through a zero-energy state that is energetically isolated from a continuum, yielding uniformly spaced Coulomb-blockade conductance peaks, consistent with teleportation via Majorana modes[16,17]. Our results help to explain the trivial-to-topological transition in finite systems and to quantify the scaling of topological protection with end-mode separation.

The set of structures we investigate consists of InAs nanowires grown by molecular beam epitaxy in the [0001] wurtzite direction with an epitaxial aluminium (Al) shell on two facets of the hexagonal cross-section[18]. The Al shell was removed except in a small segment of length L and isolated from normal metal (titanium/gold) leads by electrostatic gate-controlled barriers (Fig. 1a). The charging energies E_C of the measured devices range from greater than to less than the superconducting gap of Al (approximately 0.2 meV). The thinness of the Al shell (8–10 nm on the two facets) results in a large critical field B_c before superconductivity is destroyed: for fields along the wire axis, $B_{c,\parallel} \approx 1$ T; out of the plane of the substrate, but roughly in the plane of the two Al-covered facets, $B_{c,\perp} \approx 700$ mT (Fig. 1b). The very high critical fields that are achieved make these wires a suitable platform for investigating topological superconductivity[18].

Five devices over a range of Al shell lengths $L \approx 0.3$–1.5 μm were measured (see Methods for device layouts). Charge occupation and tunnel coupling to the leads were tuned via electrostatic gates. Differential conductance g in the Coulomb-blockade regime (high-resistance barriers) was measured using standard a.c. lock-in techniques in a dilution refrigerator (electron temperature of about 50 mK).

Figure 1c shows g as a function of gate voltage V_G and source–drain bias V_{SD}. For the $L = 790$ nm device, the zero-field data (Fig. 1c, top) show a series of evenly spaced Coulomb diamonds with a characteristic negative-differential conductance (NDC) region at higher bias. NDC is known from metallic superconductor islands[19,20] and has recently been reported in a proximitized semiconductor device similar to those investigated here[21]. The zero-magnetic-field diamonds reflect charge transport via Cooper pairs, with gate-voltage period proportional to $2e$, the charge of a Cooper pair. At moderate magnetic fields (Fig. 1c, middle), the large diamonds shrink and a second set of diamonds appears, yielding even–odd spacing of Coulomb-blockade zero-bias conductance peaks[22], as seen in the bottom panel of Fig. 1d. At larger magnetic fields (Fig. 1c, bottom), Coulomb diamonds are again periodic, but have precisely half the spacing of the zero-field diamonds, corresponding to $1e$ periodicity. At this field NDC is absent, and resonant structure is visible within each diamond, indicating transport through discrete resonances at low bias and a continuum at high bias (see magnification in Fig. 1c). Coulomb-blockade conductance peaks at high magnetic field (see Fig. 1d for zero-bias cross-sections) with regular $1e$ periodicity (half the zero-field spacing) accompanied by a discrete sub-gap spectrum are a proposed signature of electron teleportation by Majorana end states[16,17]. We designate the ungrounded tunnelling device in this high-field regime as a 'Majorana island', where a sub-gap state near zero energy, energetically isolated from a continuum, leads to $1e$-periodic Coulomb-blockade conductance peaks.

Zero-bias conductance can be qualitatively understood in a simple zero-temperature model in which the energy of the superconducting island—with or without sub-gap states (Fig. 1d)—is given by a series of shifted parabolas: $E_N(N_G) = E_C(N_G - N)^2 + p_N E_0$, in which $N_G = CV_G/e$ is the gate-induced charge (with electron charge e and gate capacitance C)[19,20,22–25] and N is the electron occupancy. E_0 is the energy of the lowest quasiparticle state, which is filled for odd parity ($p_N = 1$, odd N) and empty for even parity ($p_N = 0$, even N)[21]. Transport occurs when the ground state has a charge degeneracy, that is, when the E_N parabolas intersect. For $E_0 > E_C$, the ground state always has even parity; transport in this regime occurs via tunnelling of Cooper pairs at degeneracies of the even-N parabolas. This is the regime in which the $2e$-periodic Coulomb-blockade peaks are seen at low magnetic fields (Fig. 1d, blue). The odd charge state carries spin and its energy can be lowered by the Zeeman effect when a magnetic field is applied. For sufficiently large field, such that $E_0 < E_C$, an odd-N ground state emerges. This transition from $2e$ charging to $1e$ charging is seen experimentally as the splitting of the $2e$-periodic Coulomb diamonds into the even–odd double-diamond pattern in Fig. 1d (green). In this regime, the Coulomb-peak spacing is proportional to $E_C + 2E_0$ for even diamonds and $E_C - 2E_0$ for odd diamonds[23,24]. For the particular case of a zero-energy Majorana state ($E_0 = 0$) peak spacing is regular and $1e$-periodic. This regime

[1]Center for Quantum Devices and Station Q Copenhagen, Niels Bohr Institute, University of Copenhagen, Copenhagen, Denmark. [2]Department of Physics, Harvard University, Cambridge, Massachusetts, USA.
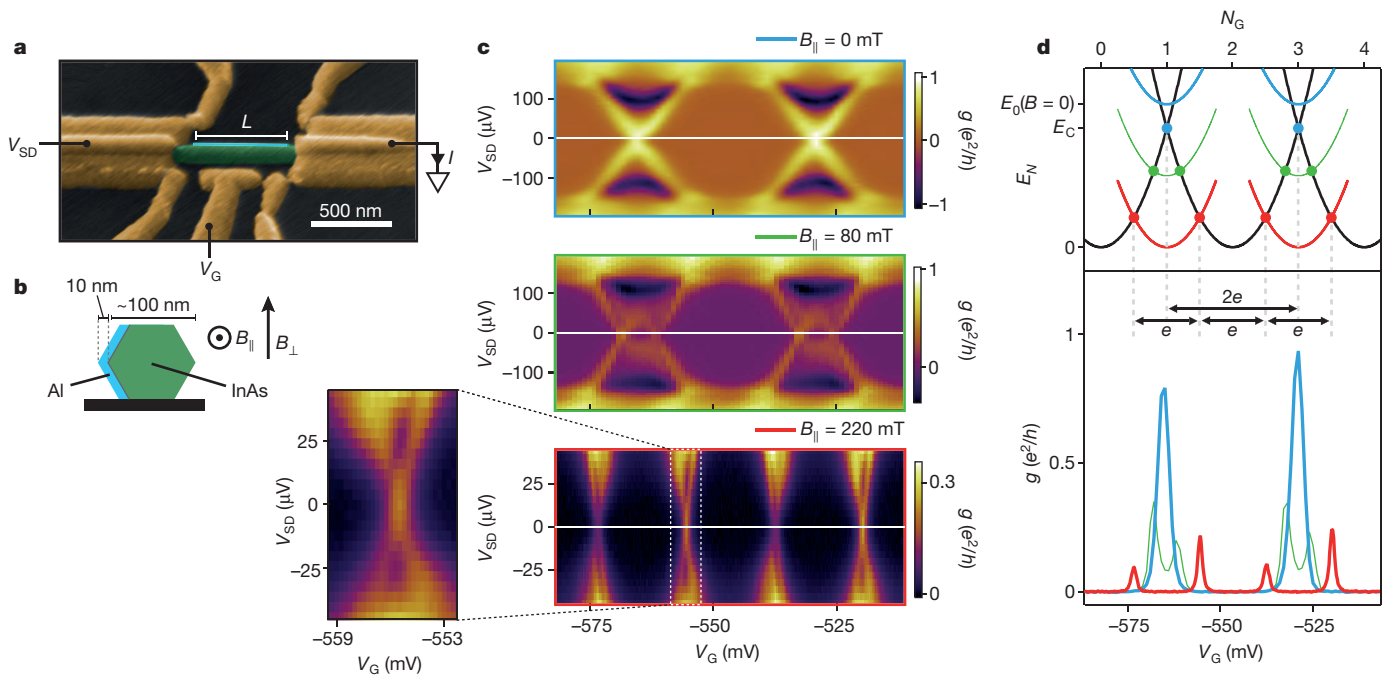*These authors contributed equally to this work.

Figure 1 | Majorana island device. a, Electron micrograph (false colour) of a device that is lithographically similar to the measured devices. Yellow, Ti/Au contacts; green, InAs nanowire; light blue, two-facet Al shell (of length L); V_{SD}, applied voltage bias; I, measured current; V_G, gate voltage. **b**, Cross-section of a hexagonal InAs nanowire showing the orientation of the Al shell and field directions $B_\parallel$ and $B_\perp$. **c**, Differential conductance $g = dI/dV_{SD}$ as a function of gate voltage V_G and source–drain bias V_{SD} for parallel magnetic fields $B_\parallel = \{0, 80, 220\}$ mT, showing a series of Coulomb diamonds. For $B_\parallel = 0$ mT, the Coulomb diamonds are evenly spaced. An odd diamond has appeared for $B_\parallel = 80$ mT. For $B_\parallel = 220$ mT, the Coulomb diamonds feature evenly spaced discrete states, but the period in gate voltage has halved compared to the $B_\parallel = 0$ mT case. Horizontal white lines indicate the locations of the plots shown in **d**. **d**, Top, energy E_N of the

device with electron occupancy N as a function of normalized gate voltage N_G. Ground-state energies for even (odd) N are shown in black (colour). Odd-N energies are raised by the single-particle-state energy E_0 relative to even-N energies. In regimes with even N only, $E_0 > E_C$ (in which E_C is the charging energy; light blue); in regimes with both even and odd N, $E_0 < E_C$ (green). The Majorana case ($E_0 = 0$) is shown in red. Transport can occur at the intersections of the parabolas, indicated by the filled circles. Bottom, differential conductance g versus gate voltage V_G at zero bias from measurements in **c** for magnetic fields $B_\parallel = \{0, 80, 220\}$ mT. The splitting of the 2e-periodic peak (light blue line) reflects a transition from Cooper pair tunnelling to single-quasiparticle charging of the Coulomb island. Evenly spaced, 1e-periodic Coulomb peaks are characteristic of a zero-energy state.

is observed at higher fields (Fig. 1d, red), although not so high as to destroy superconductivity.

Coulomb-peak spacings are measured as a function of magnetic field, allowing the state energy, $E_0(B)$, to be extracted. An example, showing ten consecutive peaks for the $L = 0.9\,\mu$m device, is shown in Fig. 2a. The peaks are 2e-periodic at $B = 0$, start splitting at $B \approx 95$ mT and become 1e-periodic at $B \approx 110$ mT, well below the spectroscopically observed closing of the superconducting gap at $B_c \approx 600$ mT (see Methods). This result indicates the presence of a state close to zero energy within the superconducting regime over a range of about 500 mT.

Separately averaging even and odd Coulomb-peak spacings ($\langle S_{e,o} \rangle$) over an ensemble of adjacent peaks reveals oscillations around the 1e-periodic value as a function of applied magnetic field. This finding is consistent with an oscillating state energy E_0 due to hybridized Majorana modes[13–15]. For the $L = 0.9\,\mu$m device (Fig. 2b), peak-spacing oscillations yield an energy oscillation amplitude $A = 7.0 \pm 1.5\,\mu$eV that is converted from gate voltage to energy using the gate lever arm η, which is extracted independently from the slope of the Coulomb diamonds. For the $L = 1.5\,\mu$m device (Fig. 2c), oscillations in the average Coulomb-peak spacing determined from 22 consecutive peaks yield a barely resolvable amplitude $A = 1.2 \pm 0.5\,\mu$eV.

Oscillation amplitudes for the five measured devices (see Methods for device details) are shown in Fig. 2d along with a two-parameter fit to an exponential function, $A = A_0 e^{-L/\xi}$, which yields $A_0 = 300\,\mu$eV and $\xi = 260$ nm as fit parameters. The data fit well to the predicted exponential form that characterizes the topological protection of Majorana modes[3,4,13].

Excited states of the Majorana island are probed using finite-bias transport spectroscopy. This technique requires a fixed gate voltage,

which is chosen such that, at zero bias, the electrochemical potential of the leads aligns with the centre of the spectroscopic gap of the Majorana island. With this choice, the conductance observed at a source–drain bias V_{SD} is due to states at energy $eV_{SD}/2$. A conductance peak at zero bias corresponds to a zero-energy state. In the case shown in Fig. 3a, b, the gate voltage is tuned using the characteristic finite-bias conductance spectra for a short InAs/Al island that was investigated previously[21]. Ground-state energies determined by finite-bias spectroscopy match those extracted from zero-bias peak spacings (see Extended Data Fig. 7).

Bias spectroscopy shows discrete zero-energy states emerging at sufficient applied field over a range of device lengths. In a short device (Fig. 3c), the discrete state moves linearly as a function of magnetic field, passing through zero and merging with a continuum at $V_{SD} \approx 100\,\mu$eV. This merging is expected for Majorana systems in the short-length limit, in which quenching of spin–orbit coupling results in unprotected parity crossings and state intersections at high energy[14]. However, rather than passing directly through zero, the first zero crossing extends for 40 mT; this behaviour is not understood. For medium-length devices, the sub-gap state bends back towards zero after zero crossings (Fig. 3d), in agreement with theoretical predictions for the emergence of Majorana behaviour with increasing system length[14,15]. For a long device ($L = 1.5\,\mu$m), bias spectroscopy shows a zero-energy state separated from a continuum at higher bias (Fig. 3e). The zero-energy state is present over a field range of 120 mT, with an associated energy gap of $(30\,\mu$eV$)/k_B = 0.35$ K (in which k_B is the Boltzmann constant).

The evolution with increasing device length from unprotected parity crossings to energetically isolated oscillating states and then to a fixed
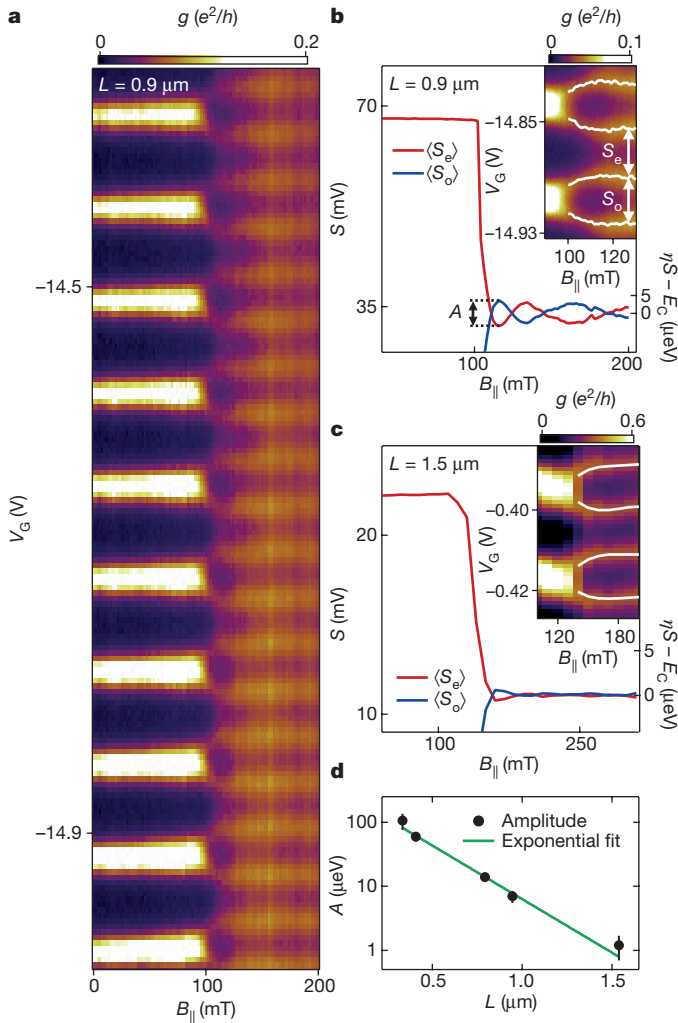
Figure 2 | Peak splitting in magnetic field. a, Zero-bias conductance g as a function of gate voltage V_G and parallel magnetic field $B_\parallel$ for the $L = 0.9\,\mu m$ device, showing a series of $2e$-periodic Coulomb peaks below about 100 mT and nearly $1e$-periodic peaks above about 100 mT. **b**, Average peak spacing for even and odd Coulomb valleys $\langle S_{e,o}\rangle$ from the measurement shown in **a** as a function of magnetic field $B_\parallel$. The Coulomb peaks become evenly spaced at $B_\parallel = 110$ mT; at higher fields, their spacing oscillates around $\langle S_e\rangle = \langle S_o\rangle$. The right axis shows the energy scale $\eta S - E_C \propto E_0$ in the $1e$-periodic regime (η is gate lever arm; see text). Inset, high-resolution measurement for $L = 0.9\,\mu m$ (**a**) with the peak centre overlaid. Even and odd peak spacings $S_{e,o}$ are indicated by the arrows. **c**, As for **b**, but for a longer wire, $L = 1.5\,\mu m$. **d**, Oscillatory amplitude A plotted against the shell length L for 5 devices (L ranging from 330 nm to 1.5 μm; black dots). The green line is an exponential fit to the data: $A = A_0\exp(-L/\xi)$ with $A_0 = 300\,\mu eV$ and $\xi = 260$ nm. Error bars indicate uncertainties propagated from lever-arm measurements and fits to peak maxima.

zero-energy state is consistent with the expected crossover from a strongly overlapping precursor of split Majorana states to a topologically protected Majorana state locked at zero energy[14,15]. In the data in Fig. 3e, the signal from the discrete state disappears for $B_\parallel > 320$ mT. This is not expected for a simple (disorder-free, single sub-band) Majorana picture. Even though the zero-bias peak disappears, the peak spacing remains $1e$-periodic (see Methods).

The observed effective g-factors of 20–50, which are extracted from the addition spectrum and bias spectroscopy (see Methods), are large compared to previous studies on InAs nanowires[9,26,27], perhaps as a result of field focusing from the Al shell. The measured gap to the continuum at zero magnetic field is consistent with the gap of aluminium, $\Delta_{Al} \approx 180\,\mu eV$, and is roughly the same in all devices. The discrete subgap states (Fig. 3c–e) have zero-field energy that is less than,
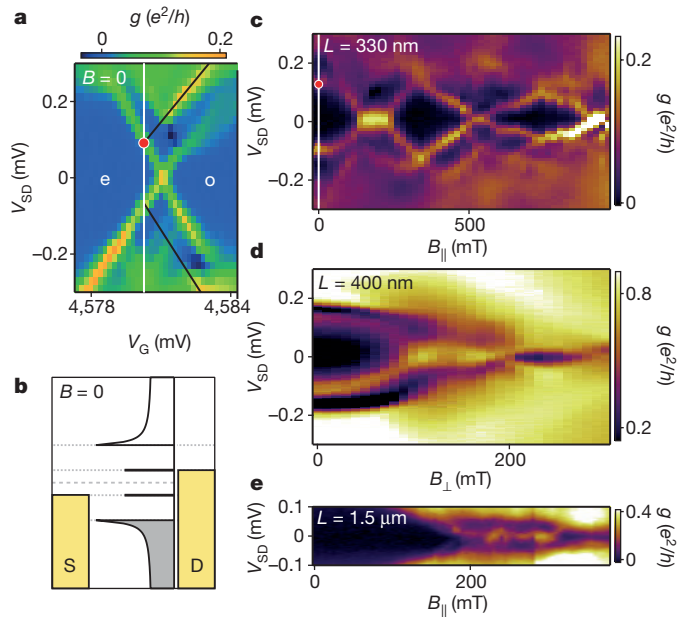

Figure 3 | Bias spectroscopy. a, Conductance g versus bias voltage V_{SD} and gate voltage V_G for the $L = 330$ nm device. Black lines indicate conductance due to a bound state; red marker is at $eV_{SD} = 2E_0$. 'e' and 'o' indicate regions in which the electron occupancy N is even and odd, respectively. **b**, Coulomb island and lead density of states at the voltage configuration indicated by the red marker in **a**. Changing the voltage bias moves the marker along the white line in **a**. 'S' and 'D' indicate the source and the drain, respectively. Shading indicates occupied states. **c–e**, Conductance g versus source–drain bias V_{SD} and magnetic field $B_\parallel$ (**c**, **e**) or $B_\perp$ (**d**) for the $L = 330$ nm (**c**), $L = 400$ nm (**d**) and $L = 1.5\,\mu m$ (**e**) devices with the gate voltage V_G equivalent to the position indicated schematically for $L = 330$ nm by the white line in **a**.

but comparable to, the gap, $E_0(B = 0) \approx 50$–$160\,\mu eV$, which is consistent with expectations for half-shell geometries[28]. The measured gap between the near-zero-energy state and the continuum in the high-field (topological) regime, $\Delta_T \approx 30\,\mu eV$, as well as the coherence length extracted from the exponential fit to the length-dependent splitting (Fig. 2d), $\xi \approx 260$ nm, are consistent with topological superconductivity. At low magnetic fields, the gap and coherence length are related to the strength of spin–orbit coupling: $\alpha_{SO} \approx \xi \times \Delta_T = 8 \times 10^{-2}\,eV\,\text{Å}$; this value is consistent with those previously reported for InAs nanowires[9,29]. For a single sub-band, this implies a Fermi velocity $v_F = \alpha_{SO}/\hbar = 1 \times 10^4\,m\,s^{-1}$ that is lower than expected, suggesting that more than one sub-band is occupied under the Al shell; however, we are not able to extract the number of modes directly.

Finally, we consider the magnetic-field dependence of the heights of Coulomb-blockade peaks (as opposed to the spacings) (Fig. 4). We found in most devices that below the field B^*, at which $2e$-periodic peaks split, all peaks had uniformly high amplitude. Above B^*, peak heights rapidly decreased and remained low up to a second characteristic field, B^{**}, coincident with the onset of $1e$ periodicity (that is, the field at which even–odd spacing differences vanished). Above B^{**}, peak heights recovered. In the longer wires, peaks were nearly absent between B^* and B^{**} (Fig. 4c).

We interpret these observations as follows. In the present lead–wire–lead geometry, transport at fields above B^* involves single electrons entering one end of the wire and leaving from the other. The onset of uniform spacing with the reappearance of high peaks for fields above B^{**} indicates the emergence of a state (or states) at zero energy with strong wavefunction weight at both ends of the wire. This is consistent with teleportation of electrons from one end of the wire to the other via a Majorana mode[16,17], although it is not necessarily a unique signature of teleportation[30]. Therefore, although the simultaneous brightening of peaks and their becoming uniformly spaced at B^{**} suggests a sub-gap or Majorana mode moving to the ends of the wire as it moves to zero
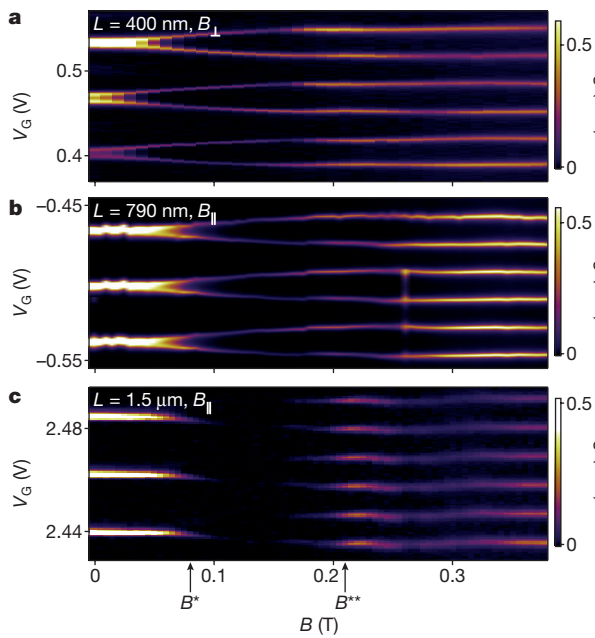
Figure 4 | Length dependence of Coulomb-peak heights.
a–c, Conductance g as a function of magnetic field $B_\perp$ (**a**) or $B_\parallel$ (**b**, **c**) and gate voltage V_G for device lengths $L = 400$ nm (**a**), $L = 790$ nm (**b**) and $L = 1.5\,\mu$m (**c**). Coulomb peaks become dim at field B^* and brighten at field B^{**}, particularly for the $L = 1.5\,\mu$m device, consistent with teleportation at fields above B^{**}.

energy, we cannot rule out other forms of end-localized zero-energy states that could appear above a critical field.

In summary, we studied Majorana islands composed of InAs nanowires covered on two facets with epitaxial Al, for a range of device lengths. Zero-energy states are observed for wires of all lengths away from zero field. Oscillating energy splittings, measured using Coulomb-blockade spectroscopy, are exponentially suppressed with wire length, with a characteristic length $\xi = 260$ nm. This result constitutes an explicit demonstration of exponential protection of zero-energy modes. Finite-bias measurements show transport through a discrete zero-energy state, with a measured topological gap $\Delta_T = 30\,\mu$eV for long devices. The extracted Δ_T and ξ are consistent with known parameters for InAs nanowires and the emergence of topological superconductivity. Brightening of Coulomb peaks at the field at which spacing becomes uniform for longer devices suggests the presence of a robust delocalized state connecting the leads, and provides experimental support for electron teleportation via Majorana modes.

Online Content Methods, along with any additional Extended Data display items and Source Data, are available in the online version of the paper; references unique to these sections appear only in the online paper.

Received 14 September 2015; accepted 18 January 2016.

1. Kitaev, A. Y. Fault-tolerant quantum computation by anyons. *Ann. Phys.* **303**, 2–30 (2003).
2. Nayak, C., Simon, S. H., Stern, A., Freedman, M. & Das Sarma, S. Non-Abelian anyons and topological quantum computation. *Rev. Mod. Phys.* **80**, 1083–1159 (2008).
3. Read, N. & Green, D. Paired states of fermions in two dimensions with breaking of parity and time-reversal symmetries, and the fractional quantum Hall effect. *Phys. Rev. B* **61**, 10267–10297 (2000).
4. Kitaev, A. Y. Unpaired Majorana fermions in quantum wires. *Phys. Usp.* **44**, 131–136 (2001).
5. Lutchyn, R. M., Sau, J. D. & Das Sarma, S. Majorana fermions and a topological phase transition in semiconductor-superconductor heterostructures. *Phys. Rev. Lett.* **105**, 077001 (2010).
6. Oreg, Y., Refael, G. & von Oppen, F. Helical liquids and Majorana bound states in quantum wires. *Phys. Rev. Lett.* **105**, 177002 (2010).
7. Mourik, V. et al. Signatures of Majorana fermions in hybrid superconductor-semiconductor nanowire devices. *Science* **336**, 1003–1007 (2012).
8. Rokhinson, L. P., Liu, X. & Furdyna, J. K. The fractional a.c. Josephson effect in a semiconductor–superconductor nanowire as a signature of Majorana particles. *Nature Phys.* **8**, 795–799 (2012).
9. Das, A. et al. Zero-bias peaks and splitting in an Al–InAs nanowire topological superconductor as a signature of Majorana fermions. *Nature Phys.* **8**, 887–895 (2012).
10. Deng, M. T. et al. Anomalous zero-bias conductance peak in a Nb–InSb nanowire–Nb hybrid device. *Nano Lett.* **12**, 6414–6419 (2012).
11. Churchill, H. O. H. et al. Superconductor-nanowire devices from tunneling to the multichannel regime: zero-bias oscillations and magnetoconductance crossover. *Phys. Rev. B* **87**, 241401 (2013).
12. Nadj-Perge, S. et al. Observation of Majorana fermions in ferromagnetic atomic chains on a superconductor. *Science* **346**, 602–607 (2014).
13. Das Sarma, S., Sau, J. D. & Stanescu, T. D. Splitting of the zero-bias conductance peak as smoking gun evidence for the existence of the Majorana mode in a superconductor-semiconductor nanowire. *Phys. Rev. B* **86**, 220506 (2012).
14. Stanescu, T. D., Lutchyn, R. M. & Das Sarma, S. Dimensional crossover in spin-orbit-coupled semiconductor nanowires with induced superconducting pairing. *Phys. Rev. B* **87**, 094518 (2013).
15. Rainis, D., Trifunovic, L., Klinovaja, J. & Loss, D. Towards a realistic transport modeling in a superconducting nanowire with Majorana fermions. *Phys. Rev. B* **87**, 024515 (2013).
16. Fu, L. Electron teleportation via Majorana bound states in a mesoscopic superconductor. *Phys. Rev. Lett.* **104**, 056402 (2010).
17. Hützen, R., Zazunov, A., Braunecker, B., Yeyati, A. L. & Egger, R. Majorana single-charge transistor. *Phys. Rev. Lett.* **109**, 166403 (2012).
18. Krogstrup, P. et al. Epitaxy of semiconductor–superconductor nanowires. *Nature Mater.* **14**, 400–406 (2015).
19. Hekking, F., Glazman, L., Matveev, K. & Shekhter, R. Coulomb blockade of two-electron tunneling. *Phys. Rev. Lett.* **70**, 4138–4141 (1993).
20. Hergenrother, J., Tuominen, M. & Tinkham, M. Charge transport by Andreev reflection through a mesoscopic superconducting island. *Phys. Rev. Lett.* **72**, 1742–1745 (1994).
21. Higginbotham, A. P. et al. Parity lifetime of bound states in a proximitized semiconductor nanowire. *Nature Phys.* **11**, 1017–1021 (2015).
22. Eiles, T. M., Martinis, J. M. & Devoret, M. H. Even-odd asymmetry of a superconductor revealed by the Coulomb blockade of Andreev reflection. *Phys. Rev. Lett.* **70**, 1862–1865 (1993).
23. Tuominen, M. T., Hergenrother, J. M., Tighe, T. S. & Tinkham, M. Experimental evidence for parity-based 2e periodicity in a superconducting single-electron tunneling transistor. *Phys. Rev. Lett.* **69**, 1997–2000 (1992).
24. Lafarge, P., Joyez, P., Esteve, D., Urbina, C. & Devoret, M. H. Measurement of the even-odd free-energy difference of an isolated superconductor. *Phys. Rev. Lett.* **70**, 994–997 (1993).
25. Matveev, K. A., Glazman, L. I. & Shekhter, R. I. Effects of charge parity in tunneling through a superconducting grain. *Mod. Phys. Lett. B* **08**, 1007–1026 (1994).
26. Csonka, S., Hofstetter, L., Freitag, F. & Oberholzer, S. Giant fluctuations and gate control of the g-factor in InAs nanowire quantum dots. *Nano Lett.* **8**, 3932–3935 (2008).
27. Schroer, M. D., Petersson, K. D., Jung, M. & Petta, J. R. Field tuning the g factor in InAs nanowire double quantum dots. *Phys. Rev. Lett.* **107**, 176811 (2011).
28. Cole, W. S., Das Sarma, S. & Stanescu, T. D. Effects of large induced superconducting gap on semiconductor Majorana nanowires. *Phys. Rev. B* **92**, 174511 (2015).
29. Fasth, C., Fuhrer, A., Samuelson, L., Golovach, V. N. & Loss, D. Direct measurement of the spin-orbit interaction in a two-electron InAs nanowire quantum dot. *Phys. Rev. Lett.* **98**, 266801 (2007).
30. Sau, J. D., Swingle, B. & Tewari, S. Proposal to probe quantum nonlocality of Majorana fermions in tunneling experiments. *Phys. Rev. B* **92**, 020511 (2015).

Author Contributions P.K., T.S.J. and J.N. developed the nanowire materials. S.M.A. fabricated the devices. S.M.A., A.P.H. and M.M. carried out the measurements with input from F.K., T.S.J. and C.M.M. Data analysis was done by S.M.A., A.P.H. and M.M. All authors contributed to interpreting the data. The manuscript was written by S.M.A., A.P.H. and C.M.M. with suggestions from all other authors.

METHODS

Sample preparation. The InAs nanowires with epitaxial Al shells were grown via a two-step process by molecular beam epitaxy. First, the InAs nanowires were grown using the vapour–liquid–solid method with Au as a catalyst at 420 °C. Second, after cooling the system to −30 °C, the Al was grown on two facets of the hexagonal cross-section[18]. Afterwards, the nanowires were deposited on degenerately doped Si substrates with 100–500-nm-thick thermal oxides using either wet or dry deposition techniques. Wet deposition involves sonicating a growth substrate of nanowires in methanol for a few seconds, then putting several drops of the nanowire–methanol solution onto the chip surface using a pipette. Dry deposition was done by bringing a small piece of cleanroom wipe in touch with the growth substrate, then swiping it onto the chip surface. We found that although wet deposition results in a more uniform dispersion of nanowires on the chip surface, dry deposition is faster and less wasteful with nanowires. Selective removal of the Al shell was done by patterning etch windows using electron beam lithography on both sides of the nanowire, plasma cleaning the surface of the nanowire using oxygen, then etching the Al using a Transene Al Etchant D with an etching time of 10 s at 50 °C. Depending on the device, ohmic contacts to the InAs core were fabricated using either ion milling or sulphur passivation to remove surface oxides. Ion milling was done for times ranging from 85 s to 110 s using a Kaufman & Robinson KDC 40 4-CM DC Ion Source with an acceleration voltage of 120 V and an ion beam current density of 0.5 mA cm⁻² at the chip surface. Sulphur passivation was done using a 2.1% solution of $(NH_4)_2S$ in de-ionized water with 0.15 M dissolved elemental sulphur at 40 °C for 20 min. This was followed by the deposition of 5 nm of Ti as a sticking layer and 70–100 nm of Au for the ohmic contact. We found that ion milling resulted in more stable devices. Side and plunger gates were lithographically defined in the same fabrication step as were the ohmic contacts to increase device yield. PMMA was used as resist in all lithography steps.

Device geometries. Gate patterns of the five measured devices are shown in Extended Data Fig. 1. With the exception of the $L = 0.9\,\mu m$ device, all measurements involving gate dependence are tuned through resonances using the plunger gate on either the Al side or the uncoated InAs side. For the $L = 0.9\,\mu m$ device, the lower-left side gate is used to tune through resonances of the Coulomb island, because the central plunger gate was not bonded during the cool down.

Measurements. Transport measurements were carried out in an Oxford Triton dilution refrigerator with a base electron temperature of $T \approx 50\,mK$ and a 6-1-1 T vector magnet. Differential conductance $g = dI/dV_{SD}$ was measured using the a.c.-lock-in technique with an excitation voltage in the range 2–6 μV.

Peak spacing data summary. The exponential curve in Fig. 2d is derived from even–odd peak-spacing measurements in the high critical field directions, $B_\parallel$ and $B_\perp$, summarized in Extended Data Fig. 2. Suppression of spacing fluctuations with increased device length is clearly visible. The measured amplitude A is indicated by black arrows in the insets of Extended Data Fig. 2, and the values are recorded in Extended Data Table 1 for each device length, along with charging energies and lever arms.

For $L = 330\,nm$, Coulomb-peak fluctuations became uncorrelated after several peaks. To obtain a large statistical ensemble, fluctuations were averaged over five sets of Coulomb peaks taken in different device tunings. Extended Data Fig. 2a shows data from a single set of peaks; Extended Data Table 1 reports the full ensemble average.

In a transverse magnetic field applied in the low critical field direction B_{tr}, shown in Extended Data Fig. 2f-i, the oscillations are absent, with the exception of an initial overshoot for $L = 0.9\,\mu m$ at $B_{tr} = 55\,mT$ (Extended Data Fig. 2i) before the system is driven into the normal state at $B_{tr} \approx 65\,mT$.

Magnetic field orientation. The direction of the nanowire on the chip was found by orienting the magnetic field from a vector magnet in the chip plane and spectroscopically measuring the anisotropy of the critical magnetic field. By comparing to the wire direction on the basis of optical and electron micrographs, we estimate an angular precision of ±3°.

Critical field measurements. The observed $2e$-to-$1e$ splitting at $B_\parallel \approx 95\,mT$ is compared to the closing of the superconducting gap at a considerably higher critical field ($B_{c,\parallel}$) in Extended Data Fig. 3. Bias spectroscopy in Extended Data Fig. 3b shows a closing of the superconducting gap at $B_{c,\parallel} \approx 600\,mT$, more than 500 mT after the onset of evenly spaced $1e$-periodic Coulomb peaks. The change from $2e$ to $1e$ periodicity at $B_\parallel \approx 100\,mT$ in Extended Data Fig. 3a coincides with a reduction in the measured Coulomb gap in Extended Data Fig. 3b, reflecting the transition from Cooper-pair charging (which has an energy penalty of $2E_C$) to single-electron charging (which has an energy penalty of E_C). The measurement in Extended Data Fig. 3b was taken in a Coulomb valley at the gate voltage $V_G = -14.92\,V$.

Averaging of peak spacings. In Fig. 2b we show the extracted average peak spacing for several even and odd Coulomb valleys. A high-resolution measurement of the $2e$-to-$1e$ splitting is shown in Extended Data Fig. 4a. The spacings of individual even and odd valleys ($S_{e,o}$ in Extended Data Fig. 4b) exhibit the same oscillating

behaviour as the averages ($\langle S_{e,o} \rangle$), but show a small deviation from them between 100 mT and 125 mT, which might be attributable to g-factor fluctuations for successive charge occupations of the Coulomb island. Below 100 mT, the fluctuations are very small, giving an indication of instrumental noise in the measurement.

Angle dependence. The angle dependence of the anti-crossing of the state with the continuum for $L = 400\,nm$ is shown in Extended Data Fig. 5. We focus on magnetic fields B_α with angles α in the plane perpendicular to the nanowire direction. The measurements show a pronounced anti-crossing between the sub-gap state and an excitation continuum ($\alpha = 112.5°$ and $\alpha = 135°$) that is substantially reduced for $\alpha = 67.5°$. Interpreting angle dependence is complicated by the anisotropy of the g-factor and the critical field. The critical field is maximized for $\alpha = 120°$, and is reduced drastically for near-perpendicular field alignment ($\alpha = 22.5°$). The observed g-factors are highly dependent on field orientation and device tuning. For the $L = 400\,nm$ device shown in Extended Data Fig. 5, we found an approximately sinusoidal variation in g-factor by a factor of 2, with maximum g-factor occurring near $\alpha = 90°$.

Choice of gate voltage for bias spectroscopy. For bias spectroscopy, the gate voltage is fixed either by interpreting Coulomb diamonds, as discussed in the main text, or from even–odd peak spacings. Although details of the bias spectroscopy, such as locations of zero-crossing, depend on the choice of gate voltage, general features such as slopes, typical fluctuation amplitude and the presence of a robust excitation gap are not strongly affected by the choice of gate voltage (Extended Data Fig. 6).

Comparison of addition energies and finite-bias spectroscopy. Peak spacings are used to measure the energy of the lowest-lying state. The same information is present in the bias spectroscopy, and gives consistent results, as shown in Extended Data Fig. 7.

Bias spectroscopy of the long device. Common-mode fluctuations in Coulomb-peak position were observed in the longest ($L = 1.5\,\mu m$) device, as shown in Extended Data Fig. 8a. The fluctuations evidently correspond to a shift in the electrochemical potential of the dot, probably due to a nearby, field-dependent charge trap. The fluctuations are small compared to charging energy, but complicate the application of bias spectroscopy, which needs to be performed at fixed electrochemical potential. To correct for the fluctuations, we introduce an effective gate voltage

$$V_{G,eff}(B) = V_G + \delta V(B)$$

that removes the common-mode peak motion. The offset voltage is zero at low field, when Coulomb peaks are $2e$-periodic ($\delta V(B) = 0$ for $B \leq 175\,mT$). At high field, $\delta V(B)$ is chosen so that the reference Coulomb peak (labelled in Extended Data Fig. 8b) occurs at constant $V_{G,eff}$. All non-zero $\delta V(B)$ are listed in Extended Data Table 2.

As shown in Extended Data Fig. 8b, this procedure removes the common-mode peak motion. In the case of the $L = 1.5\,\mu m$ device, bias spectroscopy is performed at fixed $V_{G,eff}$, which allows us to infer the energy of the sub-gap state at fixed electrochemical potential.

Zero-energy state at successive Coulomb peaks. The zero-energy state is robust over many successive Coulomb peaks, as shown in Extended Data Fig. 9. The full bias spectroscopy as a function of field is also reproducible over several peaks, as shown in Extended Data Fig. 10.

Measured g-factors. As can be seen in Extended Data Fig. 11, the state energy does not linearly depend on magnetic field. A nonlinear behaviour with magnetic field is expected in the presence of strong spin–orbit coupling and a finite critical field.

If the behaviour was strictly linear, then we would expect

$$B^{**} = \frac{E_0}{E_0 - E_C}B^*$$

because the peak splitting at B^* occurs when $E_0(B = 0) - E_Z = E_C$, and because the state is at zero energy at B^{**} when $E_Z = E_0(B = 0)$, where E_Z is the Zeeman energy (see Fig. 4 for reference). The nonlinear behaviour of $E_0(B)$ at higher magnetic fields approaching B^{**} renders this approximation unsuitable for an accurate measurement of the state energy at zero field.

In the low-field regime in which the state energy varies approximately linearly with magnetic field, we calculate an effective g-factor. Using this slope it is possible to obtain a rough estimate of the state energy $E_0(B = 0)$ assuming linear behaviour and extrapolating the state energy to zero magnetic field.

For bias spectroscopy, it should be noted that for gate voltages in the middle of the spectroscopic gap (see main text), transport through a state at $V_{SD} = V_0$ indicates a state energy $E_0 = eV_0/2$. An example for $L = 330\,nm$ is shown in Extended Data Fig. 11a.

Using the addition spectrum, the state energy can be calculated from the peak spacing S using $E_0 = (\eta S - E_C)/2$. Examples of extracted effective g-factors in the linear range are shown in Extended Data Fig. 11b, c.
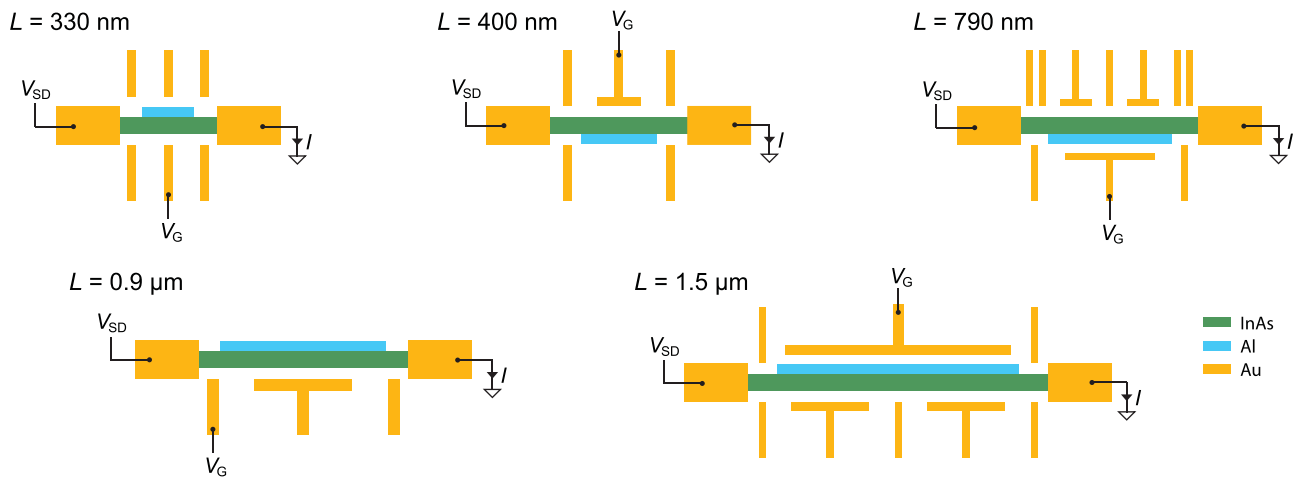
Extended Data Figure 1 | Device layouts. Gate pattern for the five measured devices showing applied voltage bias V_{SD}, measured current I and gate voltage V_G.
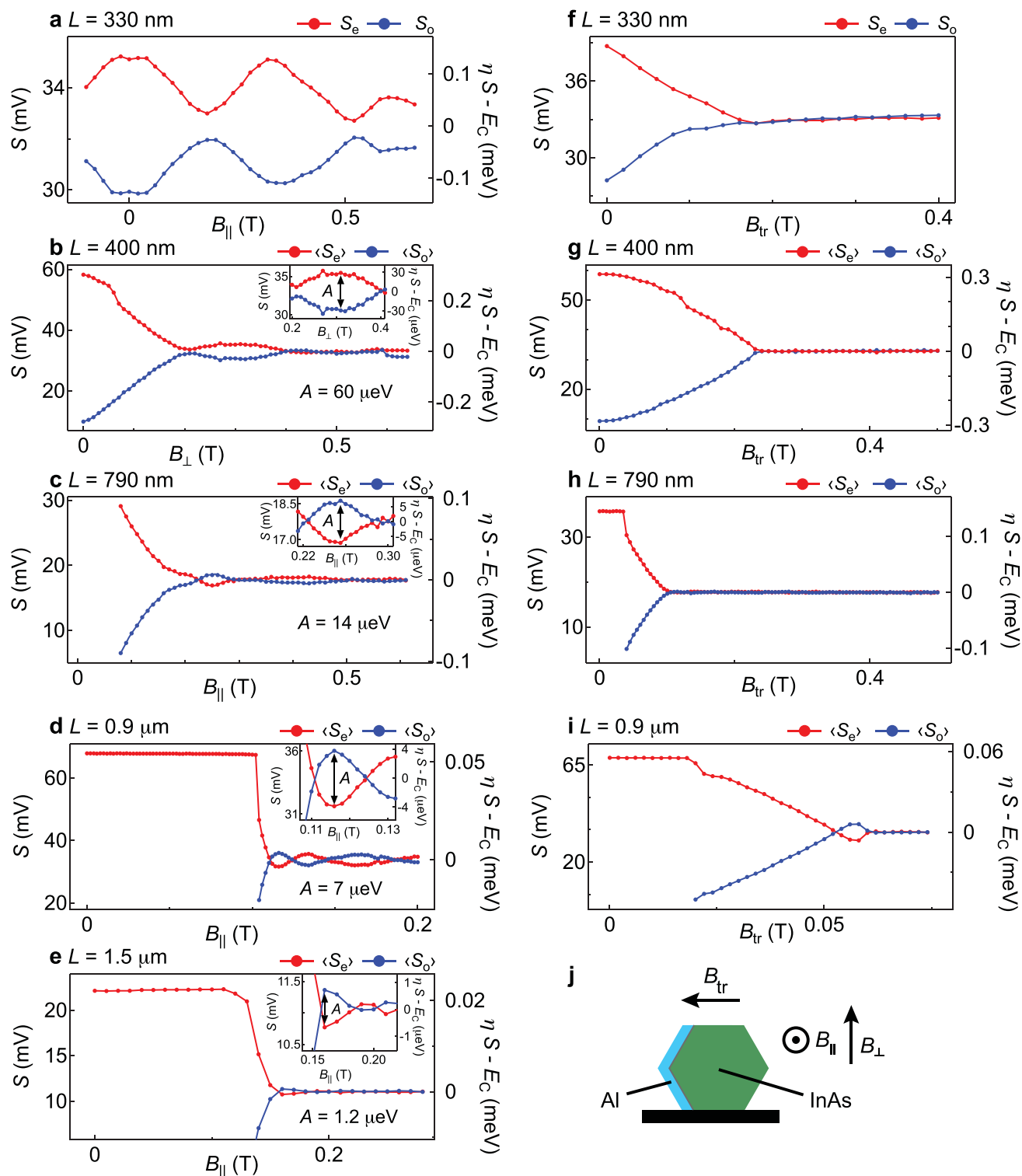
Extended Data Figure 2 | Summary of even–odd peak spacing. a–i, Peak spacings for even and odd valleys $S_{e,o}$ versus applied magnetic field $B_\parallel$, $B_\perp$ or B_{tr} (similar to Fig. 2b) for different device lengths. Left axis shows peak spacings; right axis shows corresponding energy scales, converting from gate voltage to energy by the lever arm η, which is measured independently from Coulomb-blockade diamonds. Insets show a magnification of the first energy splitting with an arrow indicating where A is measured. **j,** Cross-section of the nanowire, showing the applied field directions $B_\parallel$, $B_\perp$ and B_{tr}.
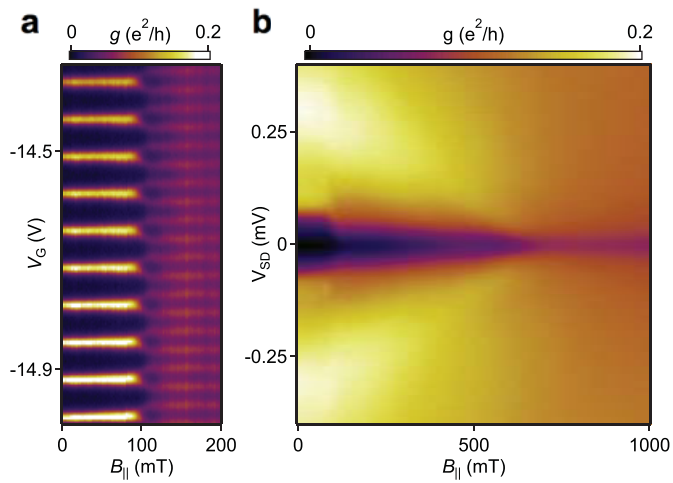
Extended Data Figure 3 | Critical field measurement for the $L = 0.9\,\mu m$ device. a, Conductance g versus gate voltage V_G and parallel magnetic field $B_\parallel$ at zero bias showing the $2e$-to-$1e$ peak splitting. **b,** Conductance versus source–drain voltage V_{SD} and $B_\parallel$, taken at $V_G = -14.92\,V$, showing a closing of the superconducting gap at $B_c \approx 640\,mT$, more than $500\,mT$ after the onset of $1e$ periodicity.
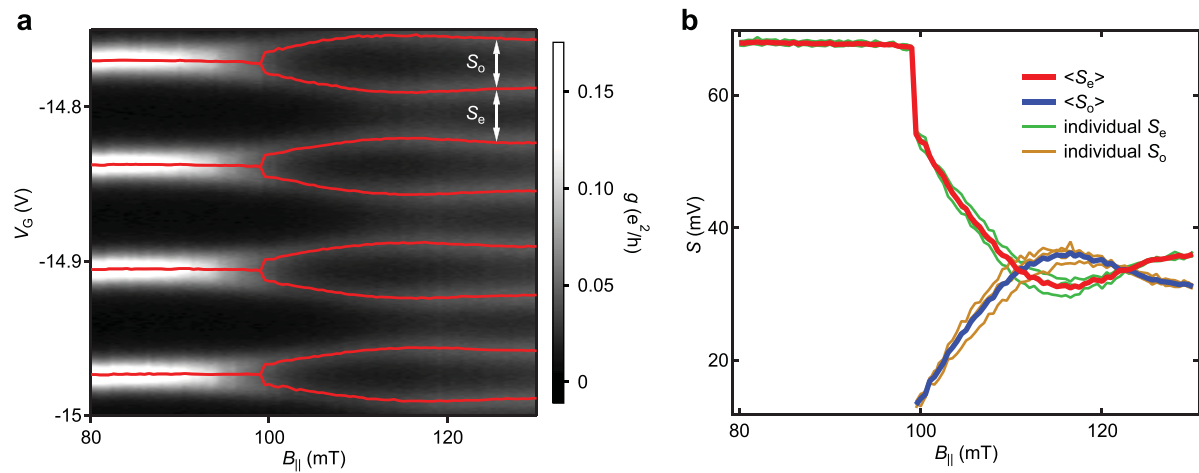
Extended Data Figure 4 | Oscillating 1*e*-periodic peak spacings. a, Zero-bias conductance *g* versus gate voltage V_G and parallel magnetic field $B_\parallel$ at zero bias showing the 2*e*-to-1*e* peak splitting for $L = 0.9\,\mu m$. The fitted peak position is indicated by a red line; even and odd peak spacings $S_{e,o}$ are indicated by white arrows. **b**, Peak spacing for even and odd valleys as a function of $B_\parallel$. The plot shows the average peak spacings $\langle S_{e,o} \rangle$ as well as the individual peak spacings $S_{e,o}$.
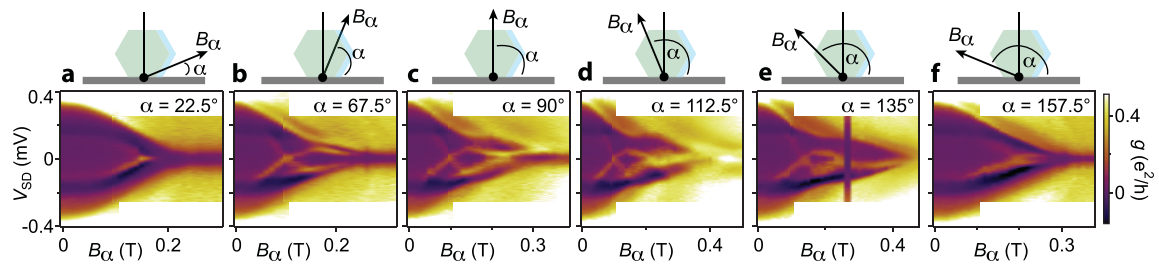
Extended Data Figure 5 | Angle dependence of state-continuum anti-crossing. a–f, Differential conductance g as a function of source–drain bias V_{SD} and magnetic field B_α for different angles ($\alpha = 22.5°–157.5°$) in the plane perpendicular to the nanowire direction. Measurements are from the $L = 400$ nm device.
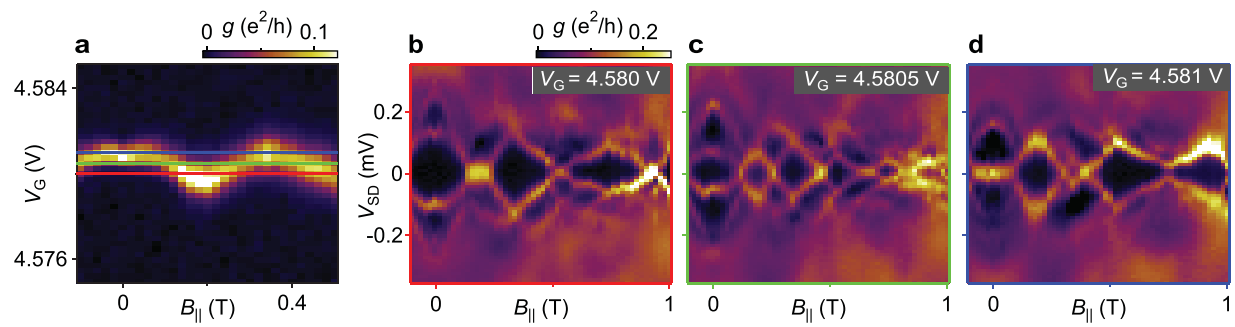
Extended Data Figure 6 | Gate positions. a, Differential conductance g as a function of gate voltage V_G and parallel magnetic field $B_\parallel$ for the $L = 330$ nm device. Three different gate positions are indicated by coloured horizontal lines. **b–d**, Differential conductance as function of bias voltage V_{SD} and $B_\parallel$ for the three gate voltages in **a**.
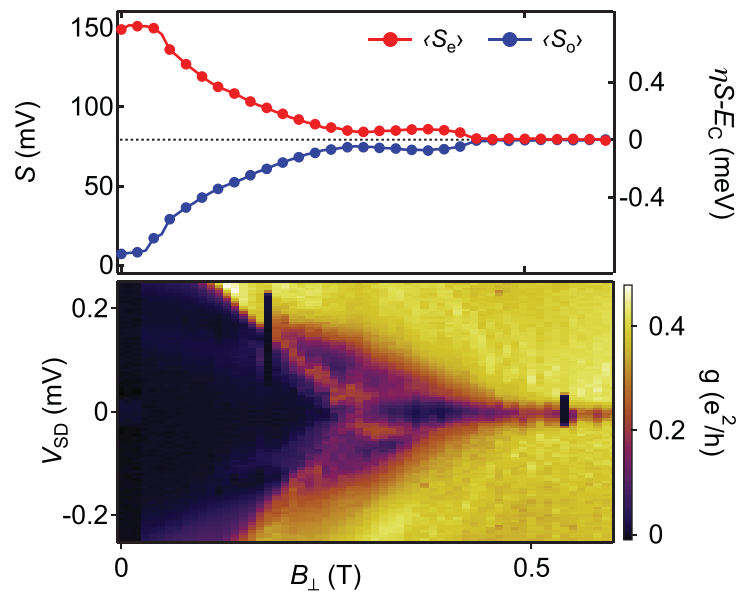
Extended Data Figure 7 | Comparison of peak spacings and bias spectroscopy. a, Peak spacing for even and odd valleys $\langle S_{e,o} \rangle$ versus applied field $B_\perp$. **b,** Differential conductance g as a function of source–drain bias V_{SD} and magnetic field $B_\perp$.
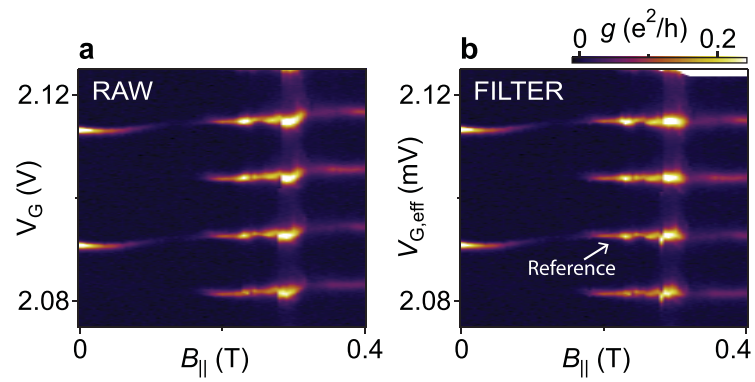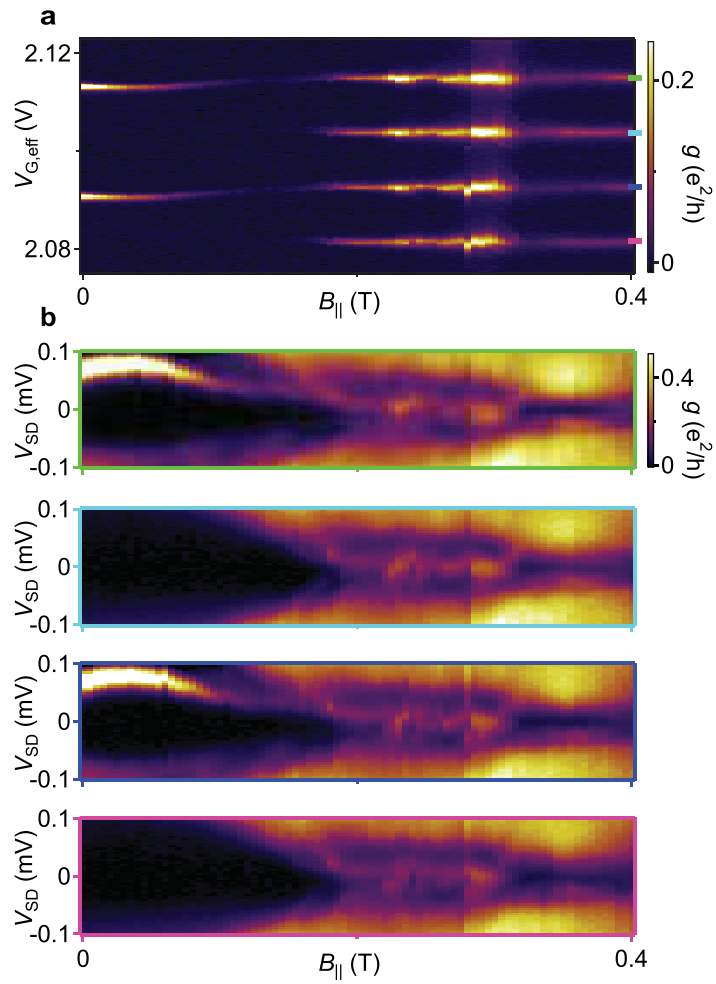
Extended Data Figure 8 | Common-mode peak motion removal. a, Differential conductance g versus gate voltage V_G and applied magnetic field $B_\parallel$ for the $L = 1.5\,\mu m$ device. **b**, Same as **a**, but with effective gate voltage $V_{G,eff}$ defined to remove common-mode peak motion. The reference Coulomb peak that is used for common-mode removal is labelled.
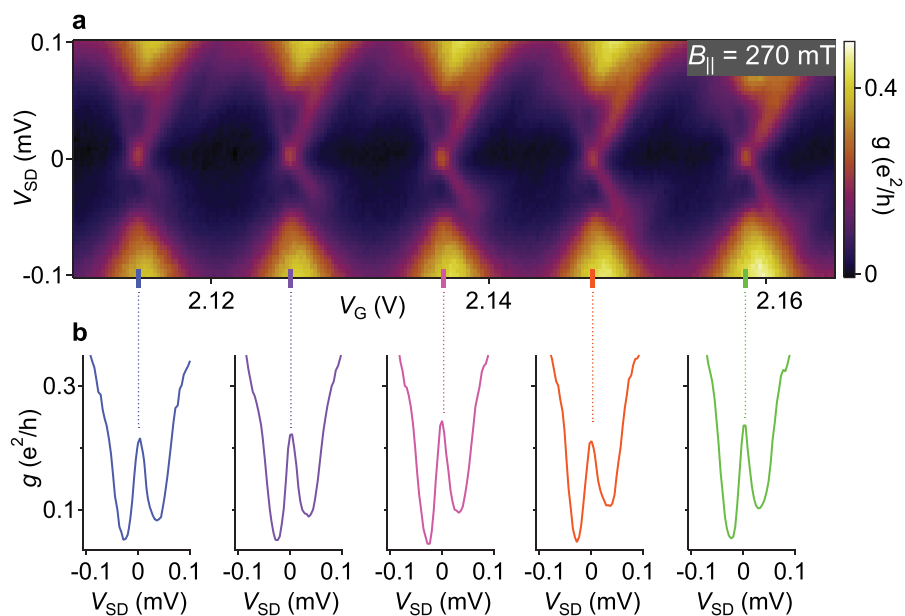
Extended Data Figure 9 | Zero-energy state. a, Differential conductance g as a function of bias voltage V_{SD} and gate voltage V_G for the $L = 1.5\,\mu m$ device and $B_{\parallel} = 270\,mT$, showing an evenly spaced Coulomb diamond pattern and the associated gapped zero-energy state. **b,** Differential conductance versus bias voltage at the gate voltages indicated by coloured ticks in **a.** At these V_G values, the presence of a zero-energy state is indicated by a zero-bias peak.

Extended Data Figure 10 | Bias-spectroscopy at successive Coulomb peaks. a, Differential conductance g versus effective gate voltage $V_{G,eff}$ and applied magnetic field $B_\parallel$. $V_{G,eff}$ is defined to remove common-mode peak motion; see Methods section 'Bias spectroscopy of the long device'. **b,** Differential conductance versus source–drain bias V_{SD} and applied magnetic field $B_\parallel$ at fixed $V_{G,eff}$ indicated by the coloured ticks on the right axis of **a**.
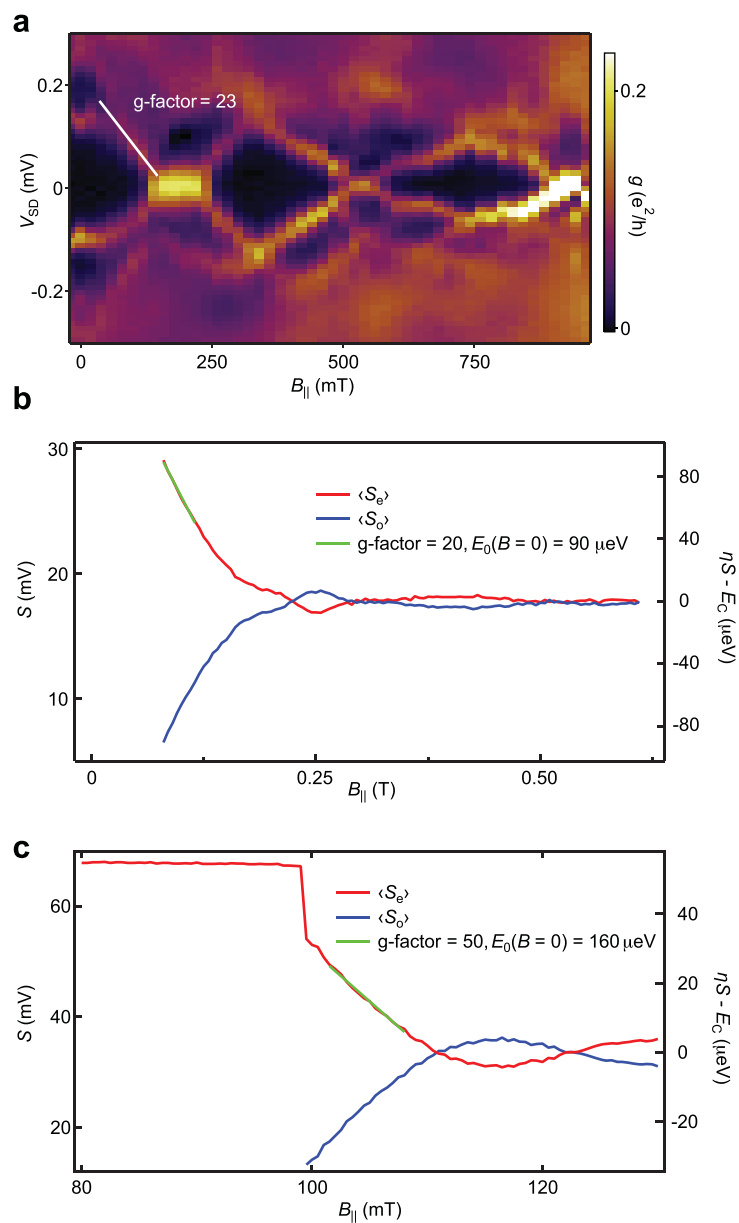
Extended Data Figure 11 | Measurement of the *g*-factor for three devices. a, Differential conductance *g* versus source–drain voltage V_{SD} and applied magnetic field $B_{\parallel}$ for the $L = 330$ nm device, showing a *g*-factor of 23. **b, c**, Average even and odd peak spacings $\langle S_{e,o} \rangle$ as a function of $B_{\parallel}$ for the $L = 790$ nm and $L = 0.9$ μm devices, showing extracted *g*-factors of 20 and 50, respectively.

Extended Data Table 1 | Device length *L*, charging energy *E*$_C$, lever arm η and characteristic amplitude *A* for the five measured devices

L [nm]	E_C [meV]	η [eV/V]	A [μeV]
330	1.6	0.048	106
400	0.40	0.012	60
790	0.14	0.008	14
950	0.054	0.0016	7
1540	0.022	0.002	1.2

Extended Data Table 2 | All non-zero offset voltage values δ$V(B)$ for the $L = 1.5\,\mu$m device

B (mT)	δV (mV)
180	0.25
230	0.25
235	0.25
240	0.25
245	0.25
250	0.25
255	0.25
260	0.5
265	0.5
270	0.5
275	0.5
280	0.75
300	0.25
305	0.75
310	1.25
315	1.5
320	1.75
325	1.75
330	1.75
335	1.75
340	1.75
345	1.75
350	1.75
355	1.75
360	1.75
365	1.75
370	1.75
375	1.75
380	1.75
385	1.75
390	1.75
395	1.75
400	1.75

Offset is defined for $B = \{0, 5, 10,..., 400\}$ mT.